Electronic Supplementary Material (ESI) for Nanoscale.
This journal is © The Royal Society of Chemistry 2022

Supplementary Information

Topochemical synthesis of Mn_2O_3/TiO_2 and $MnTiO_3/TiO_2$ nanocomposites as lithium-ion battery anode with fast Li^+ migration and giant pseudocapacitance via mesocrystalline effect

Xing Wang[a], Weijie Cheng[b], Jiaqiao Hu[a], Han Yu[c], Xingang Kong[b], Shinobi Uemura[a], Takafumi Kusunose[a], Qi Feng[a]*

[a] Department of Advanced Materials Science, Faculty of Engineering and Design, Kagawa University, 2217-20 Hayashi-cho, Takamatsu-shi, 761-0396, Japan

[b] School of Materials Science and Engineering, Shaanxi University of Science and Technology, Weiyang, Xi'an, Shaanxi, 710021, PR China

[c] College of Chemistry and Chemical Engineering, Baoji University of Arts and Sciences, Baoji, 721013, China

Corresponding Author

*Qi Feng: Department of Advanced Materials Science, Faculty of Engineering and Design, Kagawa University, 2217-20 Hayashi-cho, Takamatsu-shi, 761-0396, Japan

E-mail *address*: feng.qi@kagawa-u.ac.jp

Experimental

Characterization

The crystal structure of the samples was investigated using a powder X-ray diffractometer (Shimadzu, model XRD-6100) with Cu Kα (λ=0.1542 nm) radiation. The size and morphology of the samples were characterized by field emission scanning microscopy (FE-SEM) (Hitachi, model S-900). The chemical compositions of samples were measured using an energy dispersive X-ray spectrometer (EDS) attached to the FE-SEM at an accelerating voltage of 15 kV. Transmission electron microscopy (TEM) as well as selected-area electron diffraction (SAED) were carried out on a JEM-2100F system at 200 kV, and the powder sample was supported on a microgrid. X-ray photoelectron spectroscopy (XPS) measurements were carried out by an Axis Ultra XPS instrument with an Al Kα X-ray source, and the spectra were calibrated to the C 1s peak at 284.6 eV. N_2 adsorption-desorption experiments (NOVA 4200e, Quanta chrome Instruments, United States) were evaluated to determine the specific surface area of the samples. Electron spin resonance (ESR, Bruker A300-9.5/12) spectra were tested to observe the single-electron in the samples. Raman spectra (Renishaw-invia) with an emission wavelength of 532 nm were carried out the chemical bond of samples.

Preparation of electrode

To prepare the working electrode, the Mn_2O_3/TiO_2 or $MnTiO_3/TiO_2$ nanocomposite was mixed with acetylene black and polyvinylidene fluoride (PVDF) binder at a weight ratio of 7:2:1 in N-methyl pyrrolidone (NMP) solution to form a slurry. And then it was pasted on copper foil and dried in a vacuum oven at 80 °C for 2 days. Finally, the copper foil was divided into small disks with a diameter of 15.8 mm. Electrochemical measurements were performed using CR2032 half cells, and they were assembled in argon-filled glove box (Mbraun, Germany, O_2 and H_2O contents <0.5 ppm). Pure Li foil was used as the counter electrode, and microporous polypropylene film was applied as the separator. The solution containing 1 M $LiPF_6$ dissolved in a mixture of ethylene carbonate, ethyl methyl carbonate, and DMC (1:1:1 in volume) was used as electrolyte.

Electrochemical measurement

The galvanostatic charge/discharge tests were conducted using a battery testing system (Shenzhen, Neware, China) under different current density with a voltage range of 0.01~3 V (vs Li/Li^+). The cyclic voltammetry was conducted between 0.01 and 3.0 V at a scan rate of 0.1 mV/s and electrochemical impedance spectroscopy was performed using a CHI660E electrochemistry workstation (Shanghai Chenhua, China). Pseudocapacitance test were performed via the electrochemical workstation (Chen Hua CHI660E, Shanghai, China) with the voltage range set from 0.01 to 3.0 V (vs. Li/Li^+) and the scanning rates set from 0.1 to 1 mV/s.

Section S1: Characterization of H_2O_2-HTO

The Raman spectra of HTO and H_2O_2-HTO are shown in Fig. S1 (a). The Raman bands at around 141, 181, 267, 381, 446 and 697 cm^{-1} correspond to the Ti-O lattice vibrations within the 2D lepidocrocite-type TiO_6 octahedral host layers in HTO. However, besides from these bands, a clear Raman band at 884 cm^{-1} is observed in H_2O_2-HTO, which is attributed to the O-O bond vibration within the interlayer of H_2O_2-HTO. To further confirm the existence of H_2O_2 in H_2O_2-HTO, ESR was carried out. In Fig. S1 (b), a sharp ESR signal is detected at 336.7 mT in H_2O_2-HTO while no ESR signal at around 336.7 mT can be observed in HTO sample. The ESR signal at 336.7 mT can be attributed to the existence of Ti(IV)-O-O-H species.[1] XPS was employed also to confirm the existence of O-O bond before and after H_2O_2treatment. As shown in Fig. S1 (c) and (d). The binding energies were calibrated for specimens charging by referencing the C 1s to 284.60 eV. The O1s spectrum of HTO shows two fitted peaks. The peak at 529.91 eV is assigned to Ti-O bond in TiO_6 octahedral and the peak located at 530.93 eV suggests the existence of interlayer H_2O. After H_2O_2 treatment, the XPS spectrum show the existence of Ti-O bond, besides, the peak located at 531.90 eV belongs to the O-O bond in H_2O_2-HTO (Fig. S1 (d)).[1]

Furthermore, we measured Zeta potential of HTO before and after the H_2O_2 treatment. It is found that the Zeta potential (-41.9 mV in water system) of H_2O_2-HTO becomes more negative than that of HTO (-26.3 mV in water system) (Table S1), suggesting that the formation of Ti-O-O coordination bond can cause the increase of the negative charge density of TiO_6 octahedra layers due to the electron-donating nature of $(\text{-O-O-})^{2-}$ group.[1]

Based on the above results, it can be confirmed that Ti-O-O coordination bond is formed in H_2O_2-HTO.

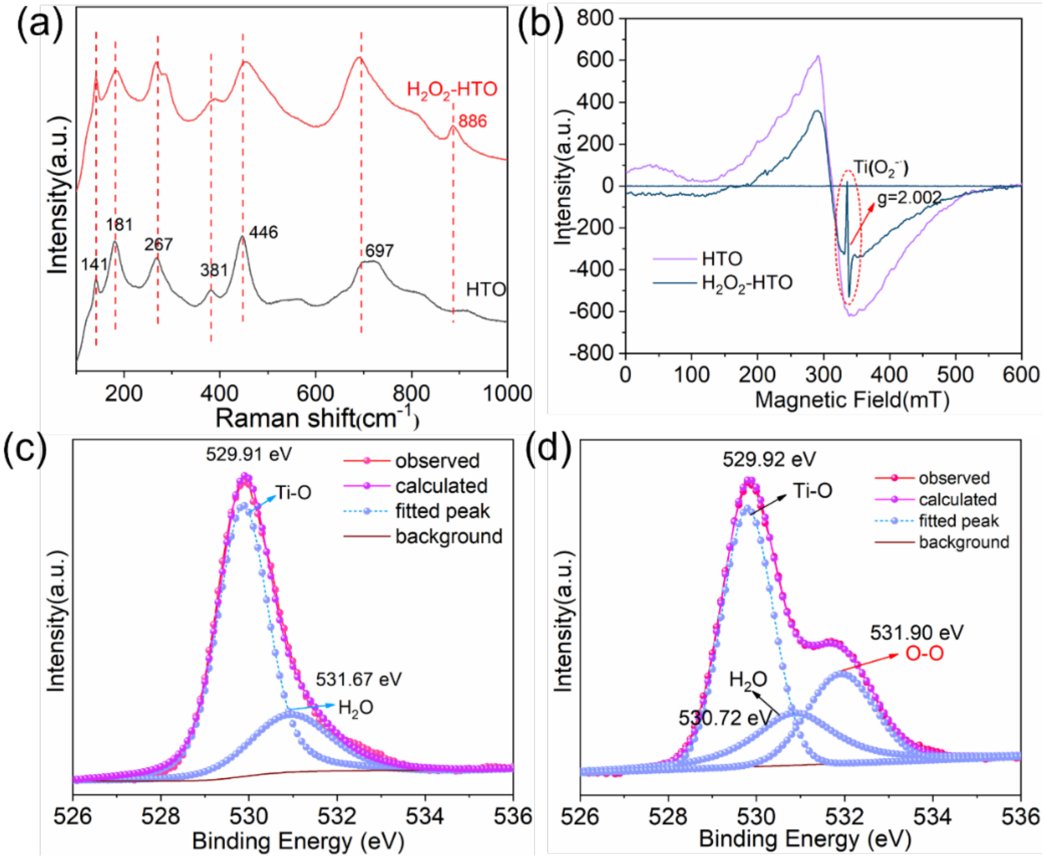

Fig. S1 (a) Raman spectra of HTO and H_2O_2-HTO, (b) ESR spectra of HTO and H_2O_2-HTO, O 1s spectrum of (c) HTO and (d) H_2O_2-HTO.

Table S1 Zeta potential of HTO before and after the H_2O_2 treatment.

Sample	**Zeta potential (mV)**
HTO	-26.3 mV (water system)
H_2O_2-HTO	-41.9 (water system)

Table S2 Molar ratios of Mn/Ti in Mn-HTO, Mn-H_2O_2-HTO, Mn-HTO-ns and Mn-H_2O_2-HTO-ns.

Samples	Mn/Ti molar ratio
Mn-HTO	0.18
Mn-H_2O_2-HTO	0.55
Mn-HTO-ns	0.26
Mn-H_2O_2-HTO-ns	0.52

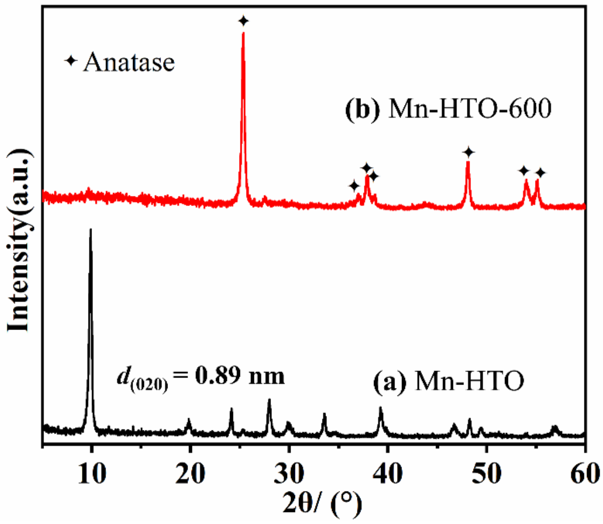

Fig. S2 XRD patterns of (a) Mn-HTO and (b) product after heat treatment of Mn-HTO at 600 °C in air.

Section S2: Synthesis of Mn_2O_3/TiO_2 nanocomposites from Mn-H_2O_2-HTO-ns

When $Mn(CH_3COO)_2$ solution was added into the HTO nanosheets colloidal solution, the nanosheets restack and a flocculated precipitate (Mn-HTO-ns) was formed immediately. XRD result indicated Mn-HTO-ns has a layered structure with a basal spacing of 0.96 nm (Fig. S3 (A) (a)). The Mn 2p XPS spectrum result suggests manganese species exist as bivalent Mn(II) in Mn-HTO-ns similar to Mn-HTO, where the energy difference of Mn $2p_{3/2}$ (641.2 eV) and Mn $2p_{1/2}$ (653.2 eV) is 12 eV (Fig. S3 (C)(a)),[2] which agrees with its yellow color (Fig. S3 (A) (a)). When $Mn(CH_3COO)_2$ solution was added into H_2O_2-HTO nanosheets (H_2O_2-HTO-ns) colloidal solution, a flocculated precipitate (Mn-H_2O_2-HTO-ns) with black color was obtained (Fig. S3 (A) (b)). Mn-H_2O_2-HTO-ns has a layered structure with a larger basal spacing of 1.17 nm than that of Mn-HTO-ns, and small amount of α-MnOOH phase was observed also in the XRD patterns (Fig. S3 (A) (b)), similar to the case of Mn-H_2O_2-HTO. However, the crystallinity of Mn-H_2O_2-HTO-ns layered phase is lower than that of Mn-H_2O_2-HTO, revealing disordering of layered structure in Mn-H_2O_2-HTO-ns. The Mn 2p XPS spectrum displays a spin energy separation of 11.7 eV between Mn $2p_{3/2}$ (642.1 eV) and Mn $2p_{1/2}$ (653.8 eV) (Fig. S3 (C)(b)), which demonstrates that Mn species exists in Mn-H_2O_2-HTO as Mn (III),[3] and Ti 2p XPS spectrum reveals valance of Ti always keeps as Ti(IV) before and after reaction with $Mn(CH_3COO)_2$ solution (Fig. S3 (D)). Based on the XRD and XPS analysis results, it can be concluded that the increased basal spacing suggests a restacking reaction of H_2O_2-HTO-ns nanosheets accompanying intercalation of Mn (III) species into the interlayer space. Except for intercalation of Mn (III) species, the redox reaction between Mn^{2+} in solution and the H_2O_2 adsorbed on the H_2O_2-HTO-ns nanosheets surface causes the formation of α-MnOOH phase on the surface of Mn-H_2O_2-HTO-ns. EDS results reveals that the Mn/Ti molar ratios in Mn-H_2O_2-HTO-ns is 0.52, higher than that of Mn-HTO-ns (Mn/Ti=0.26) (Table S2). It is due to the exfoliation H_2O_2-HTO nanosheets possess more negative charge density than that of exfoliated HTO nanosheets, which increase the Mn content in the restacked product.

When Mn-H_2O_2-HTO-ns was heat-treated, the layered structure remains up to 400 °C, along with the decrease of basal spacing caused by the dehydration of water from the interlayer space (Fig. S3 (B)), and MnO_2 phase appears at 300 and 400 °C. With heat-treatment temperature increasing, the layered structure disappeared at 500 °C, and a Mn_2O_3/TiO_2 nanocomposite was obtained above 500 °C. The Mn_2O_3 (26 wt.%) and TiO_2 (74 wt.%) contents in the Mn_2O_3/TiO_2 nanocomposite can be estimated from Mn and Ti contents in the Mn-H_2O_2-HTO-ns precursor (Table S2). The Mn 2p XPS spectrum of Mn-H_2O_2-HTO-ns-700 displays a similar result as Mn-H_2O_2-HTO-ns ((Fig. S3(C)(b) and (c)), confirming the existence of Mn(III) in Mn_2O_3/TiO_2 nanocomposite while Ti keeps tetravalent Ti(IV) before and after heat treatment ((Fig. S3(D)).

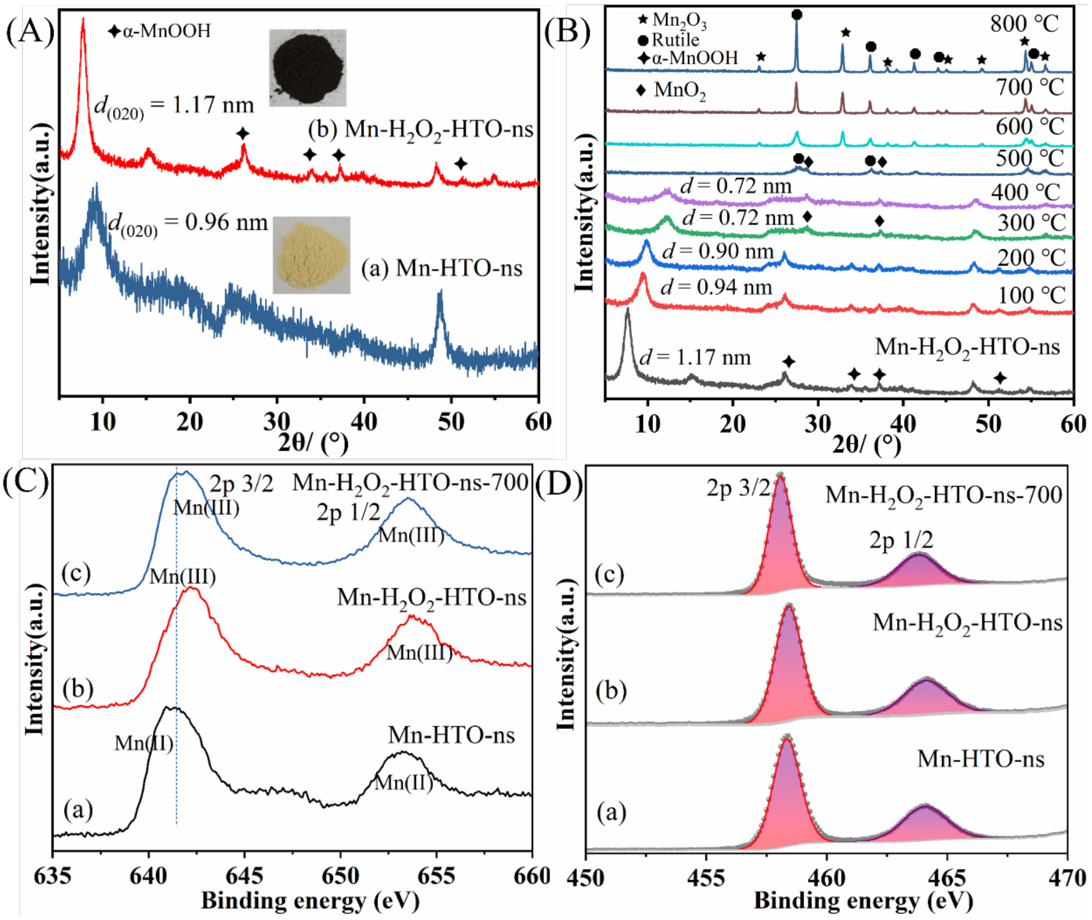

Fig. S3 (A) XRD patterns of (a) Mn-HTO-ns and (b)Mn-H_2O_2-HTO-ns; (B) XRD patterns of products obtained by heat-treating Mn-H_2O_2-HTO-ns at different temperatures in air, (C) Mn 2p and (D) Ti 2p XPS spectra of (a) Mn-HTO-ns, (b) Mn-H_2O_2-HTO-ns and (c) Mn-H_2O_2-HTO-ns-700.

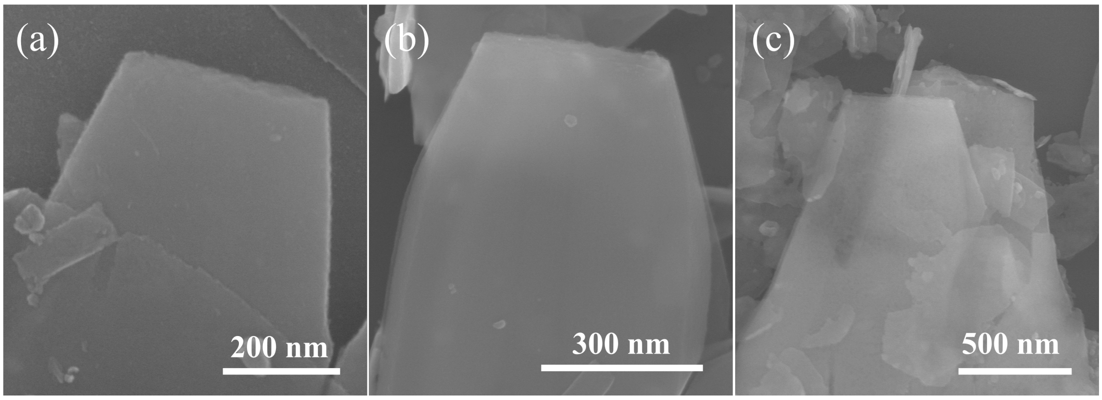

Fig. S4 FE-SEM images of (a) H_2O_2-HTO, (b) Mn-HTO and (c) products after heated Mn-HTO at 600 °C in air.

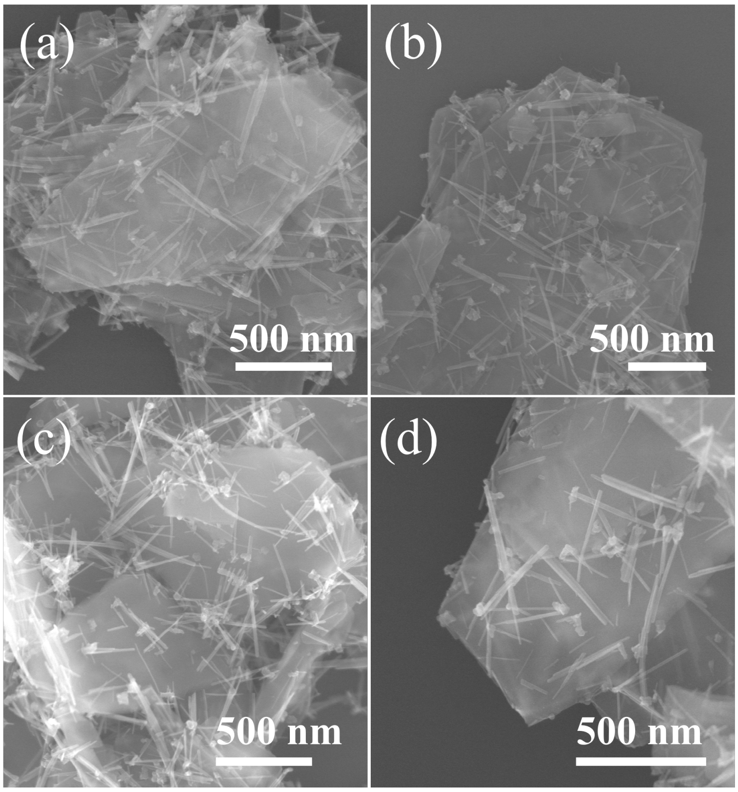

Fig. S5 FE-SEM images of products after heat treatment of Mn-H_2O_2-HTO at (a) 100, (b) 200, (c) 300 and (d) 400 °C in air.

Section S3: Particle morphologies of H_2O_2-HTO-ns, Mn-H_2O_2-HTO-ns, and Mn-H_2O_2-HTO-ns-T samples

The particle morphologies of nanosheet-assembled samples and their heat-treated products are investigated by FE-SEM, as shown in Fig. S5. H_2O_2-HTO-ns displays a nanosheetlike particle morphology with a smooth surface (Fig. S6 (a)). After assembling in Mn^{2+} solution, Mn-H_2O_2-HTO-ns shows a similar nanosheetlike particle morphology to H_2O_2-HTO with the appearance of some nanowires with the size of about 350 nm in length and 30 nm in diameter on the surface of the nanosheetlike particles (Fig. S6 (b)). The appearance of nanowires is due to formation of α-MnOOH by redox reaction between Mn^{2+} and H_2O_2 adsorbed on H_2O_2-HTO-ns nanosheet surface. When Mn-H_2O_2-HTO-ns was heat-treated, the nanosheetlike particles and nanowires on the surface keep their morphology up to 600 °C (Fig. S6(c-h)). Up to 700 °C, the nanosheet particle tends to collapse to small particles and nanowires are incorporated into the nanosheetlike particles due to the crystal growth of Mn_2O_3 and TiO_2 nanocrystals. The nanocrystal size increases from about 60 to 100 nm, when the temperature was increased from 700 to 800 °C (Fig. S6 (i) and (j)).

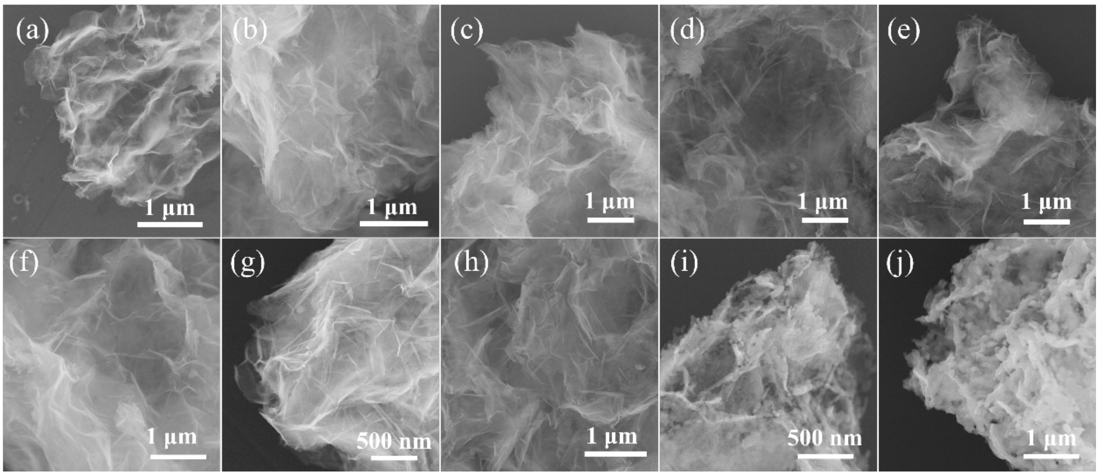

Fig. S6 FE-SEM images of products after heat treatment of (a) H_2O_2-HTO-ns, (b) Mn-H_2O_2-HTO-ns and products after heated Mn-H_2O_2-HTO-ns at (c) 100, (d) 200, (e) 300, (f) 400, (g) 500, (h) 600, (i) 700, and (j) 800 °C in air.

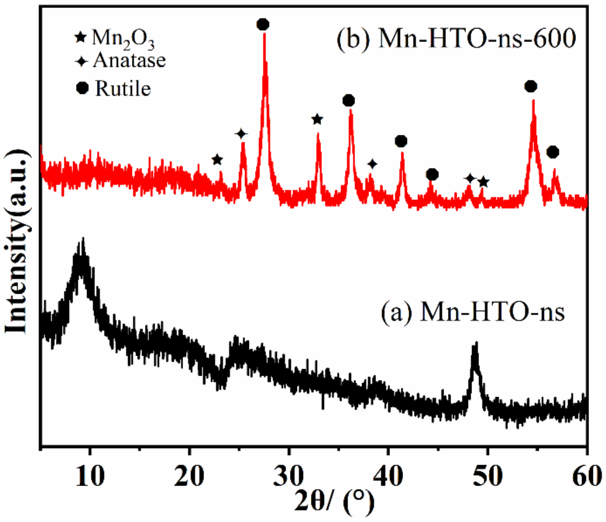

Fig. S7 XRD patterns of (a) Mn-HTO-ns and (b) product after heat-treatment of Mn-HTO-ns at 600 °C in air.

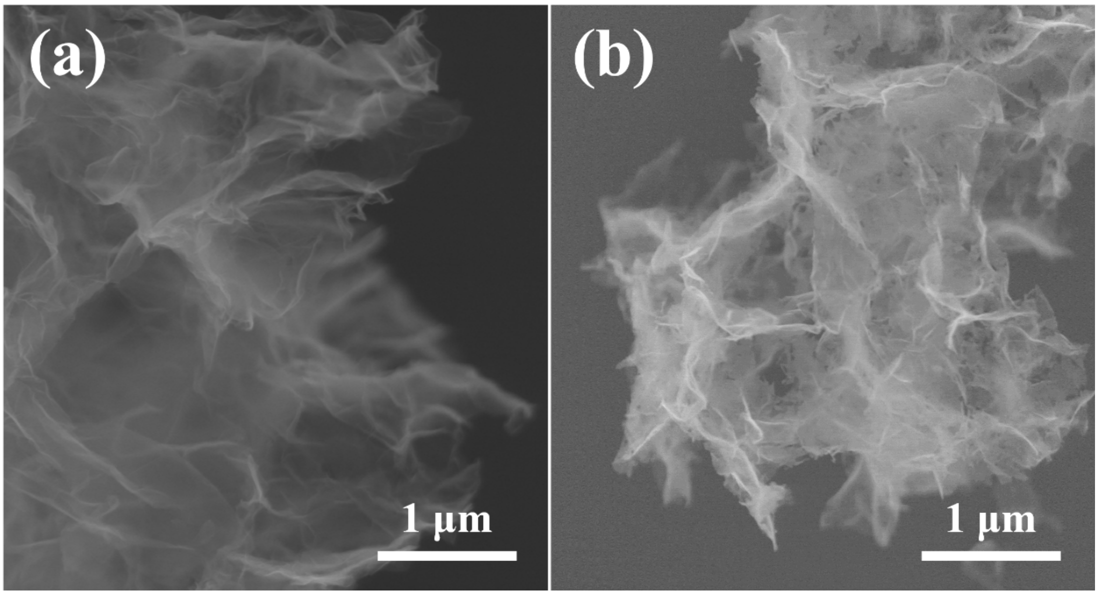

Fig. S8 FE-SEM images of (a) Mn-HTO-ns and (b) product after heat-treatment of Mn-HTO-ns at 600 °C in air atmosphere.

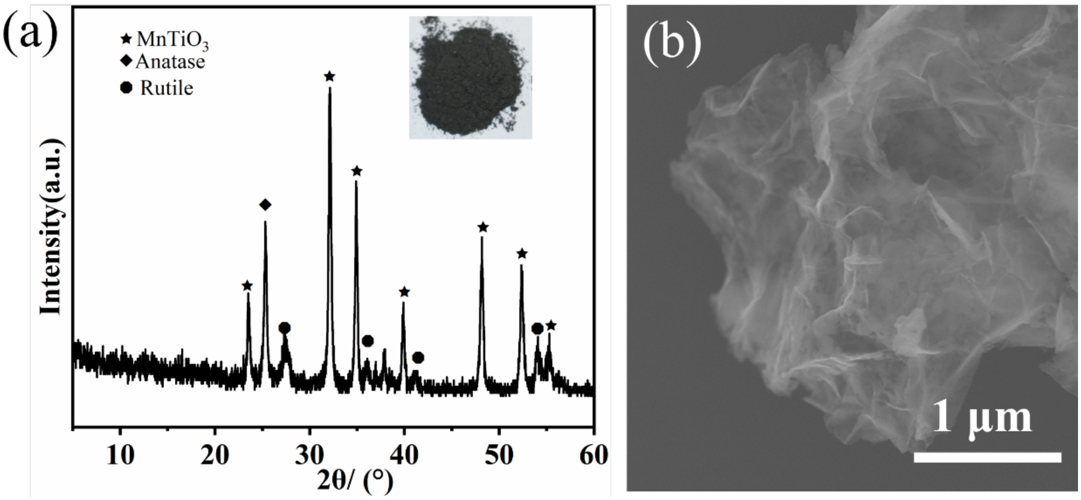

Fig. S9 (a) XRD pattern and (b) FE-SEM image of product after heat treatment of Mn-H_2O_2-HTO-ns in H_2/Ar 600 °C.

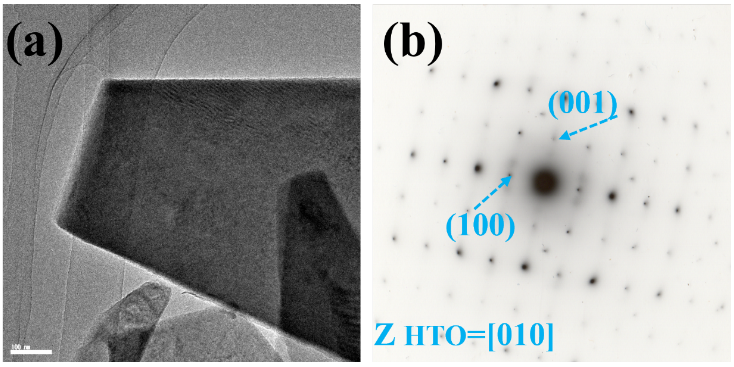

Fig. S10 (a) TEM images and (b) SAED patterns of H_2O_2-HTO.

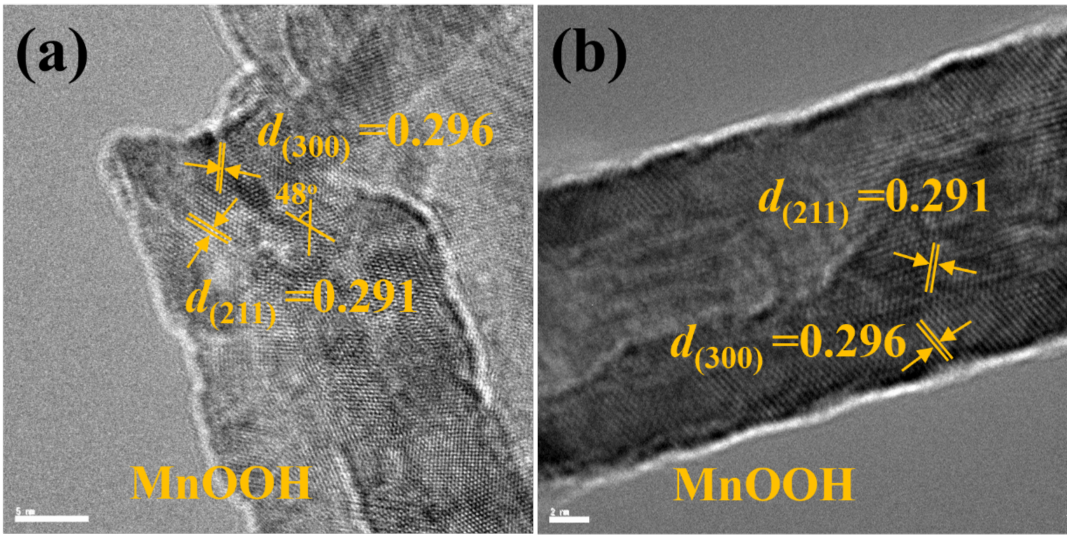

Fig. S11 HRTEM images of nanowires on the surfaces of (a) Mn-H_2O_2-HTO and (b) Mn-H_2O_2-HTO-ns.

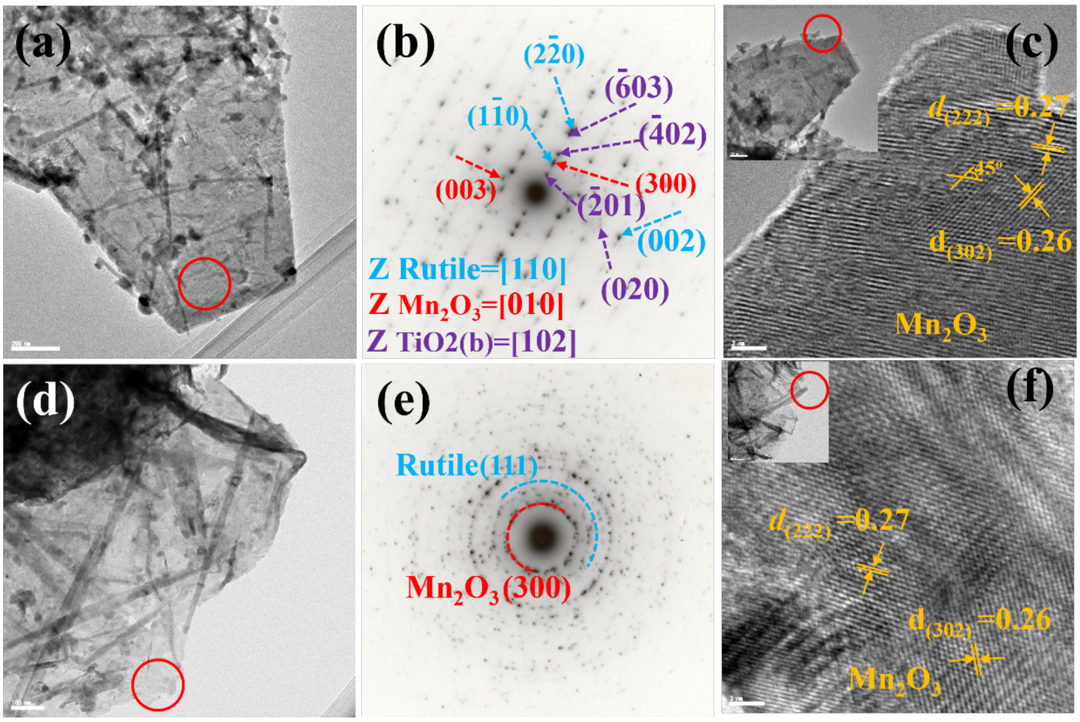

Fig. S12 TEM images, SAED patterns, HRTEM images of (a, b, c) Mn-H_2O_2-HTO-600 and (a, b, c) Mn-H_2O_2-HTO-ns-600.

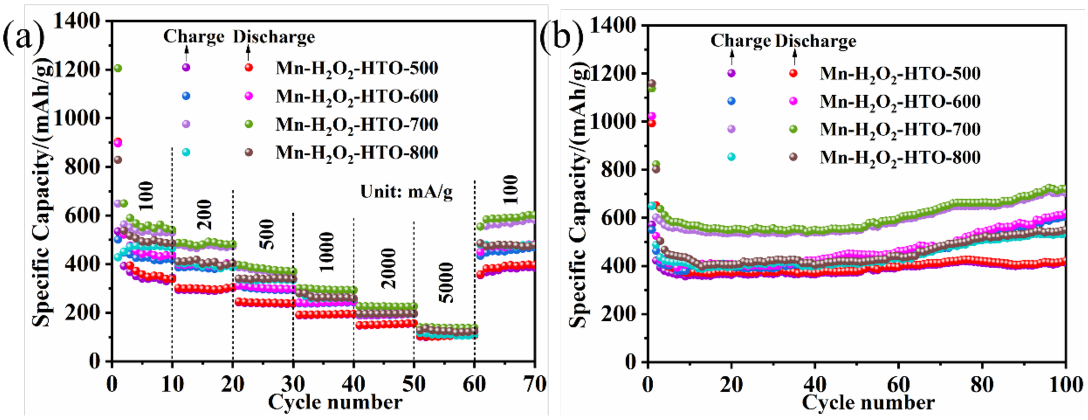

Fig. S13 (a) Rate capabilities and (b) cycling performances of Mn_2O_3/TiO_2 nanocomposites obtained by heat-treatment of Mn-H_2O_2-HTO at 500, 600, 700 and 800 °C in air, respectively.

Fig. S13 shows the discharge-charge capacity performances of mesocrystalline Mn_2O_3/TiO_2 nanocomposites obtained by heat-treatment of Mn-H_2O_2-HTO in air at different temperatures. The reversible discharge-charge specific capacity increases with increasing heat-treatment temperature, reaches maximum around 700 °C, and then decreases, as shown in Fig. S13 (a). The enhancement of discharge-charge specific capacity from the lower temperature to 700 °C can be attributed to the formation of mesocrystalline Mn_2O_3/TiO_2 nanocomposite. Although mesocrystalline Mn_2O_3/TiO_2 nanocomposite is formed in Mn-H_2O_2-HTO-800, it shows a lower capacity than that of Mn-H_2O_2-HTO-700. The Mn_2O_3 and TiO_2 nanocrystals in Mn-H_2O_2-HTO-800 are relatively large because the high heat-treatment temperature causes crystal growth of the Mn_2O_3 and TiO_2 nanocrystals, in which Li^+ are difficult to be migrated in the large Mn_2O_3 and TiO_2 nanocrystals. The above results suggest that the formation of mesocrystalline Mn_2O_3/TiO_2 nanocomposite with small crystal sizes of the Mn_2O_3 and TiO_2 nanocrystals desirable for the anode material. All these nanocomposite samples show the stable cycling performances at current density of 100 mA/g (Fig. S13 (b)).

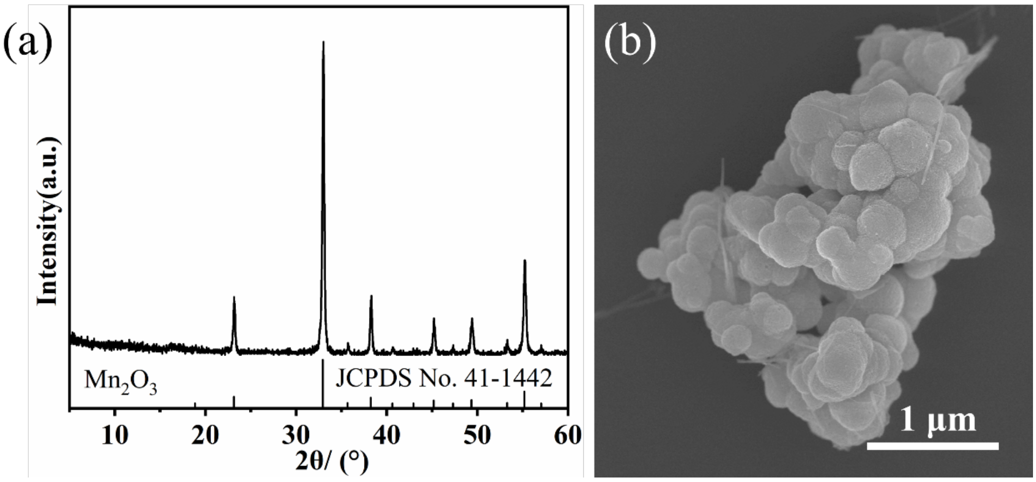

Fig. S14 (a) XRD pattern and (b) FE-SEM image of Mn_2O_3 obtained by calcining $MnCO_3$ at 700 °C for 3 h in air.

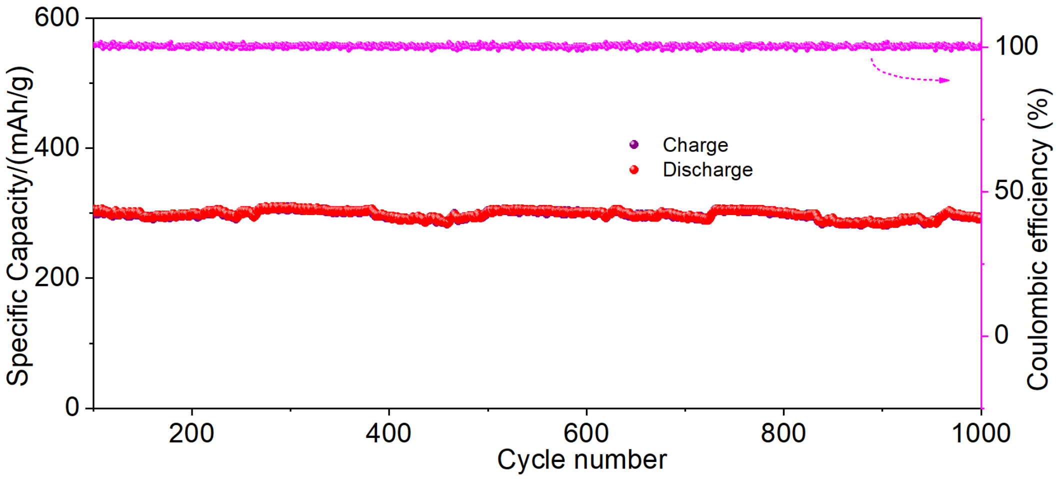

Fig. S15 Cycling performance of mesocrystalline Mn_2O_3/TiO_2 nanocomposites at 1A/g.

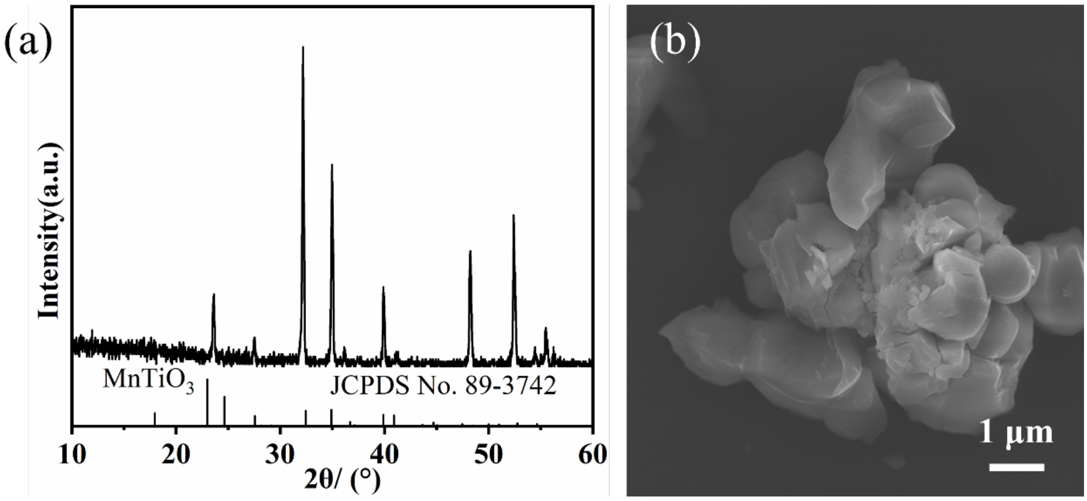

Fig. S16 (a) XRD pattern and (b) FE-SEM image of $MnTiO_3$ obtained by calcining the mixture of Mn_2CO_3 and TiO_2 at 1100 °C for 4 h in air.

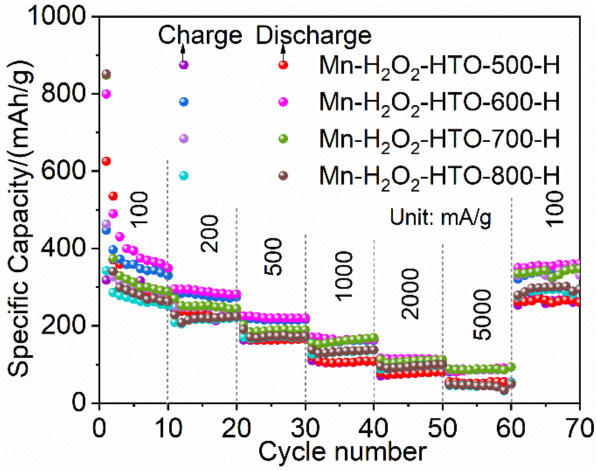

Fig. S17 Rate capabilities of mesocrystalline $MnTiO_3/TiO_2$ nanocomposites obtained by heat-treatment of Mn-H_2O_2-HTO at 500, 600, 700 and 800 °C in H_2/Ar, respectively.

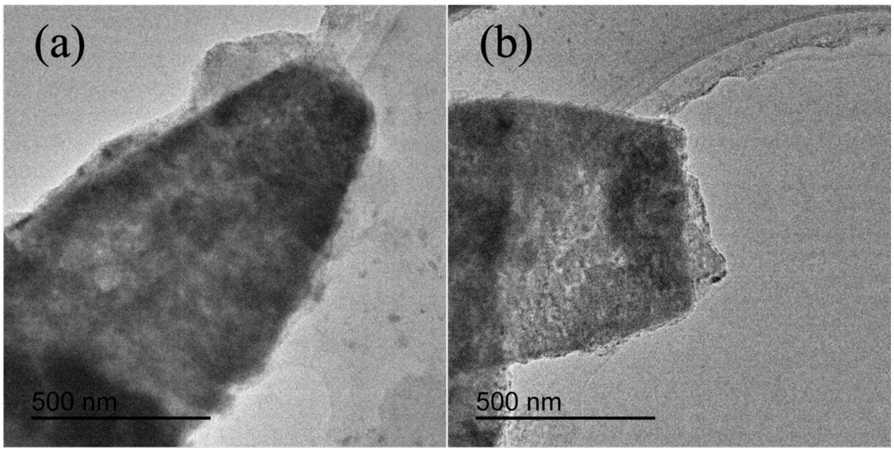

Fig. S18 *Ex-situ* TEM images of (a) mesocrystalline Mn_2O_3/TiO_2 nanocomposite (b) mesocrystalline $MnTiO_3/TiO_2$ nanocomposite after 100 cycles at 100 mA/g.

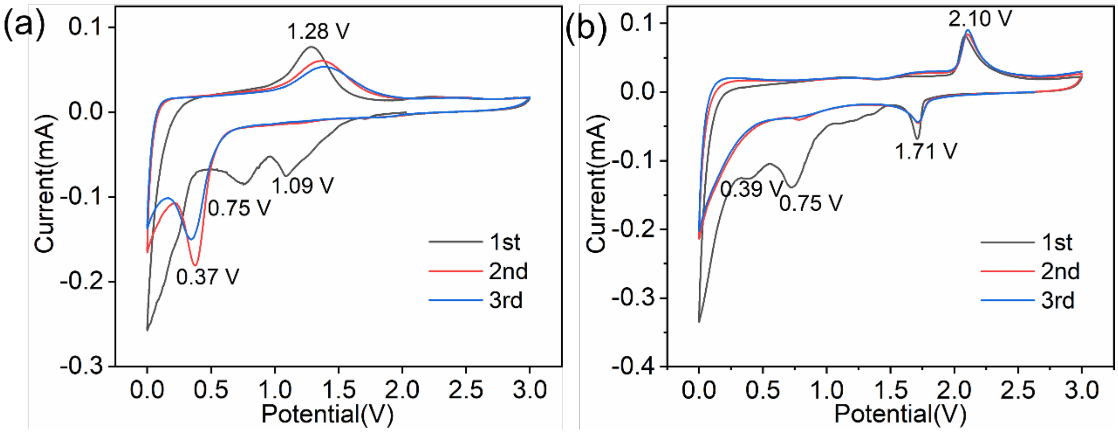

Fig. S19 Cyclic voltammetry (CV) curves of (a) mesocrystalline Mn_2O_3/TiO_2 nanocomposite (b) mesocrystalline $MnTiO_3/TiO_2$ nanocomposite at scan rate of 0.1mV/s.

Section S4: Calculation of theoretical capacities of Mn_2O_3/TiO_2 and $MnTiO_3/TiO_2$ nanocomposites

$$C(Mn_2O_3/TiO_2\ \text{theoretical}) =$$

$$C(Mn_2O_3\ \text{theoretical}) \times \text{wt\% of } Mn_2O_3 + C(TiO_2\ \text{theoretical}) \times \text{wt\% of } TiO_2 \qquad (1)$$

$$C(MnTiO_3/TiO_2\ \text{theoretical}) =$$

$$C(MnTiO_3\ \text{theoretical}) \times \text{wt\% of } MnTiO_3 + C(TiO_2\ \text{theoretical}) \times \text{wt\% of } TiO_2 \qquad (2)$$

Section S5: Measurement of pseudocapacitance

The relationship between peak current (i) and the scan rate (v) can be described as equation (3), in which b could be used to analyze the electrochemical storge mechanism of electrode materials. When the value b = 0.5, the electrochemical reaction is conducted via diffusion-controlled process, while b = 1 suggest a capacitive-controlled behavior, namely pseudocapacitance. The slope value of log (i) versus log (v) stands for the b value. The b values of peaks I and II are 0.86 and 0.69 for the mesocrystalline Mn_2O_3/TiO_2 nanocomposite (Fig. S20 (b)), respectively, indicating that electrochemical reaction concludes both the diffusion-controlled and the pseudocapacitive-controlled mechanisms. The pseudocapacitive contribution ratio could be illuminated quantitatively by equation (4), in which the k_1v and $k_2v^{1/2}$ represent capacitive behavior and diffusion contribution, respectively, and the calculated result is shown in Fig. S20 (c).

$$i = a * v^b \qquad (3)$$

$$i(V) = k_1 v + k_2 v^{1/2} \qquad (4)$$

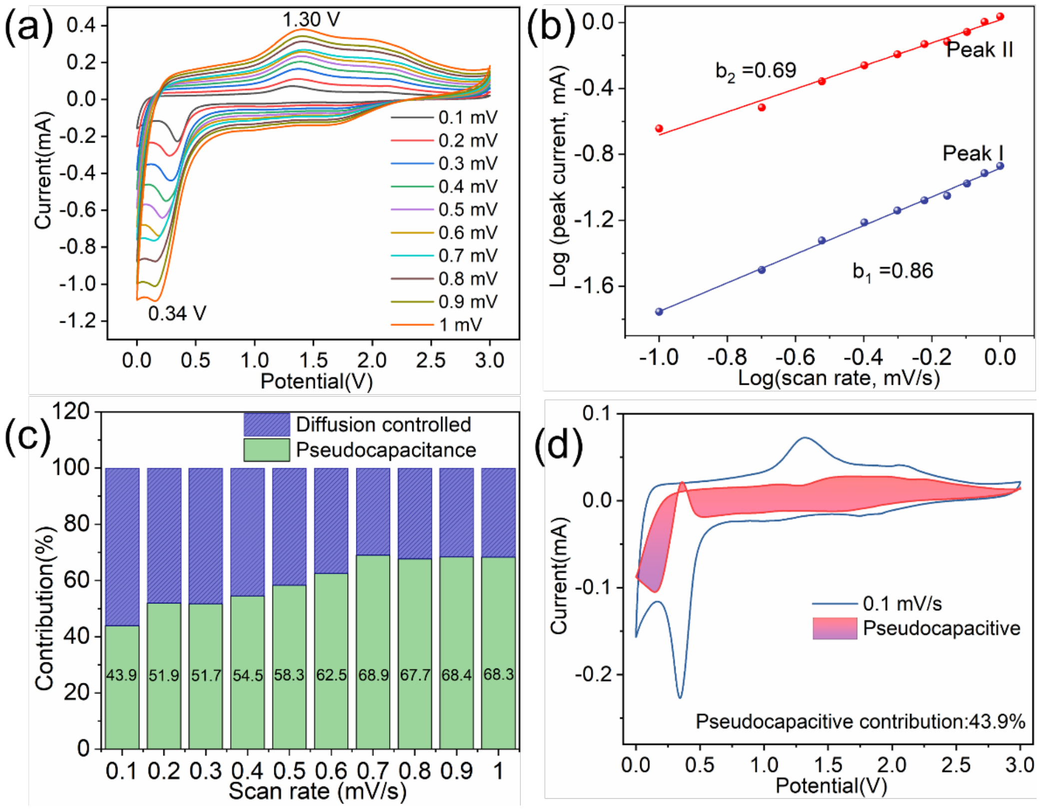

Fig. S20 (a) Cyclic voltammetry curves of mesocrystalline Mn_2O_3/TiO_2 nanocomposite at different scan rates from 0.1 to 1.0 mV s^{-1}; (b) Determination of the b-value using the relationship between peak current and scan rate; (c) Percentage of pseudocapacitive contributions at various sweep rates of mesocrystalline Mn_2O_3/TiO_2 nanocomposite; (d) CV profile of mesocrystalline Mn_2O_3/TiO_2 nanocomposite with separation between total currents (solid line) and capacitive currents (red colored regions) at a scan rate of 0.1 mV/s.

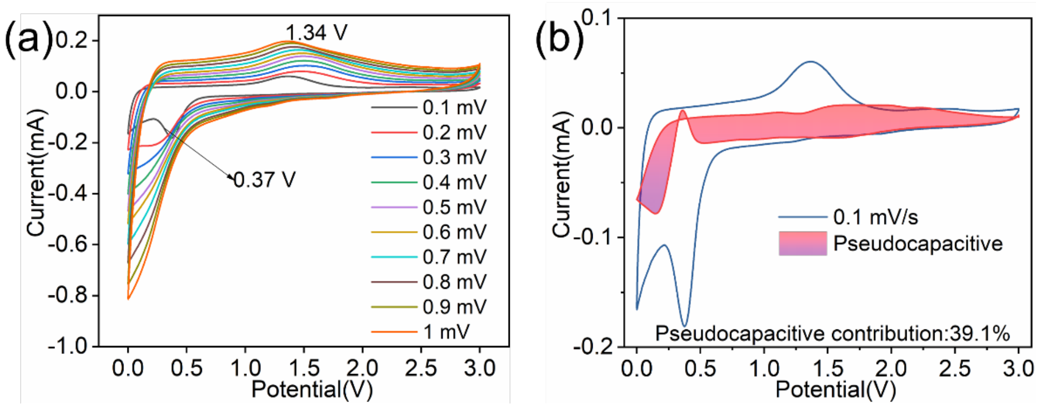

Fig. S21 (a) Cyclic voltammetry curves of polycrystalline Mn_2O_3/TiO_2 nanocomposite at different scan rates from 0.1 to 1.0 mV s^{-1}; (b) CV profile of polycrystalline Mn_2O_3/TiO_2 nanocomposite with separation between total currents (solid line) and capacitive currents (red colored regions) at a scan rate of 0.1 mV/s.

The b value of peak is 0.72 for the mesocrystalline Mn_2O_3/TiO_2 nanocomposite (Fig. S18 (b)), indicating that electrochemical reaction concludes both the diffusion-controlled and the pseudocapacitive-controlled mechanisms. The pseudocapacitive contribution ratio could be illuminated quantitatively by equation (4).

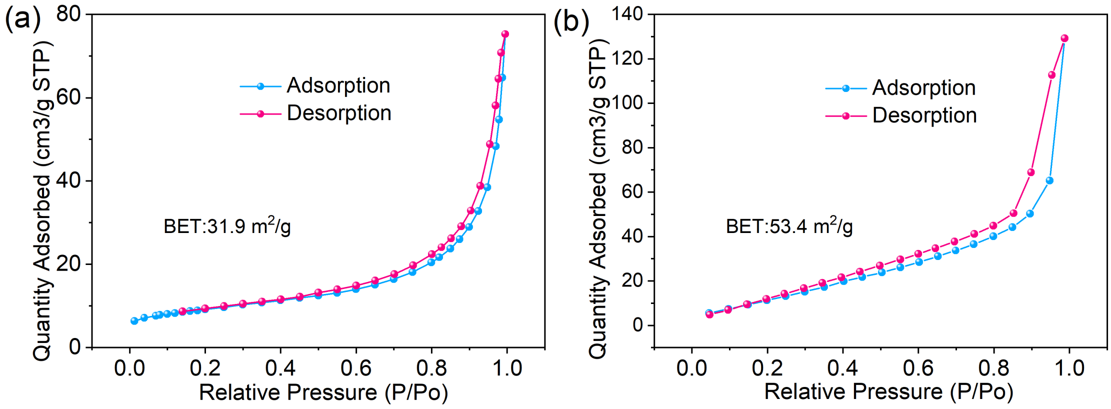

Fig. S22 Nitrogen adsorption/desorption isotherms of (a) mesocrystalline and (b) polycrystalline Mn_2O_3/TiO_2 nanocomposites.

References

1. X. Wang, W. Wei, J. Hu, S. Li, Y. Wang, L. Yin, X. Kong and Q. Feng, *ChemComm*, 2021, **57**, 7394-7397.
2. M. C. Biesinger, B. P. Payne, A. P. Grosvenor, L. W. Lau, A. R. Gerson and R. S. C. Smart, *Appl. Surf. Sci.*, 2011, **257**, 2717-2730.
3. Z. Zhou, D. Chaoying, P. Wenchao, L. Yang, Z. Fengbao and X. Fan, *J Mater. Sci. Technol.*, 2021, **80**, 13-19.